

# A comprehensive description of elastic scattering angular distributions for eight different density distribution of $^{32}\text{S}$ nucleus

T. Ulucay and M. Aygun

*Department of Physics, Bitlis Eren University, Bitlis, Turkey*

Received 21 January 2020; accepted 3 March 2020

The elastic scattering angular distributions of  $^{32}\text{S}$  projectile by  $^{12}\text{C}$ ,  $^{27}\text{Al}$ ,  $^{40}\text{Ca}$ ,  $^{48}\text{Ca}$ ,  $^{48}\text{Ti}$ ,  $^{58}\text{Ni}$ ,  $^{63}\text{Cu}$ ,  $^{64}\text{Ni}$ ,  $^{76}\text{Ge}$ ,  $^{96}\text{Mo}$  and  $^{100}\text{Mo}$  targets over the energy range 83.3 - 180 MeV are analyzed in the framework of the double folding model based on the optical model. The real part of the optical model potential is obtained by using a double folding model for eight different density distributions of  $^{32}\text{S}$ , which consist of Ngo, SP, 2pF, G1, G2, S, 3pF, and HFB. The imaginary part of the optical model potential is accepted as the Woods-Saxon (WS) potential. The theoretical results successfully reproduce the experimental data over both a wide energy range and many target nuclei. Finally, simple and useful formulas that predict imaginary potential depths of each density are derived based on the elastic scattering results.

**Keywords:** Density distribution; optical model; double folding model; elastic scattering.

PACS: 24.10.Ht; 24.50.+g; 25.70.-z

DOI: <https://doi.org/10.31349/RevMexFis.66.336>

## 1. Introduction

It is known that the element sulfur (S) has 24 isotopes. Four of them are stable;  $^{32}\text{S}$  (%94.99),  $^{33}\text{S}$  (%0.75),  $^{34}\text{S}$  (%4.25), and  $^{36}\text{S}$  (%0.01) [1]. The isotopes synthesized artificially are  $^{31}\text{S}$  and  $^{37}\text{S}$  radioisotopes, which are short-lived.  $^{32}\text{S}$  is one of the most prominent isotopes and is important in the field of both nuclear physics and nuclear medicine. For example, it is used for the production of  $^{32}\text{P}$  radioisotope evaluated for therapeutic purposes [2].

One way to examine the structure of the  $^{32}\text{S}$  nucleus is to analyze its elastic scattering data from different targets. Thus, the effective potentials can be got from the fitting of these data. Density distributions have an important place in describing elastic scattering reactions and in the evaluation of nuclear models. A large number of studies about density distributions can be found in the literature [3–7]. However, when we examine the existing densities over the  $^{32}\text{S}$  nucleus in the literature, we cannot find both a simultaneous analysis of various density distributions and global potential equations for these densities. These deficiencies induced us to consider carefully the effects of different density distributions on the elastic scattering data of the  $^{32}\text{S}$  nucleus.

In the present study, we aim at producing alternative density distributions for the  $^{32}\text{S}$  nucleus, and at obtaining new global imaginary potential equations for each density distribution. Firstly, we show eight various alternative density distributions of  $^{32}\text{S}$  projectile. Then, we calculate the elastic scattering cross-sections of  $^{32}\text{S}$  from  $^{12}\text{C}$ ,  $^{27}\text{Al}$ ,  $^{40}\text{Ca}$ ,  $^{48}\text{Ca}$ ,  $^{48}\text{Ti}$ ,  $^{58}\text{Ni}$ ,  $^{63}\text{Cu}$ ,  $^{64}\text{Ni}$ ,  $^{76}\text{Ge}$ ,  $^{96}\text{Mo}$ , and  $^{100}\text{Mo}$  targets over the energy range 83.3 - 180 MeV by using these density distributions. We compare the theoretical results with the experimental data and determine the best density distribution(s). Finally, we derive new and global potential equations that give the imaginary potential depths of the optical model potential.

Section 2 describes the calculation procedure. Section 3 displays the density distributions of projectile and targets.

Section 4 is devoted to the results and discussion. Section 5 states the summary and conclusions.

## 2. Calculation procedure

The potential of nucleus-nucleus interaction can be parameterized by

$$U(r) = V_c(r) + V(r) + iW(r) \quad (1)$$

where  $V_c(r)$ ,  $V(r)$ , and  $W(r)$  are the Coulomb, real and imaginary potentials, respectively. The  $V_c(r)$  potential is taken as [8]

$$V_c(r) = \frac{1}{4\pi\epsilon_0} \frac{Z_P Z_T e^2}{r}, \quad r \geq R_c \quad (2)$$

$$= \frac{1}{4\pi\epsilon_0} \frac{Z_P Z_T e^2}{2R_c} \left( 3 - \frac{r^2}{R_c^2} \right), \quad r < R_c \quad (3)$$

$$R_c = 1.25(A_P^{1/3} + A_T^{1/3}), \quad (4)$$

The  $V(r)$  potential is obtained for eight different densities of the  $^{32}\text{S}$  nucleus by using the double folding potential given by

$$V(\vec{r}) = \int d\vec{r}_1 \int d\vec{r}_2 \rho_P(\vec{r}_1) \rho_T(\vec{r}_2) \nu_{NN} \times [\vec{r} - (\vec{r}_1 - \vec{r}_2)], \quad (5)$$

where  $\rho_{P(T)}(\vec{r}_{1(2)})$  is the density of projectile(target), and  $\nu_{NN}$  is nucleon-nucleon interaction. The densities of projectile and targets are shown in the following subsection. The  $\nu_{NN}$  expression is

$$\begin{aligned} \nu_{NN}(r) = & \alpha_1 \frac{e^{-\alpha_2 r}}{\alpha_2 r} - \alpha_3 \frac{e^{-\alpha_4 r}}{\alpha_4 r} \\ & - 276 \left[ 1 - 0.005 \frac{E_{\text{Lab}}}{A_p} \right] \delta(r), \end{aligned} \quad (6)$$

where the values of constants  $\alpha_1$ ,  $\alpha_2$ ,  $\alpha_3$ , and  $\alpha_4$  are 7999 MeV,  $4.0 \text{ fm}^{-1}$ , 2134 MeV and  $2.5 \text{ fm}^{-1}$ , respectively. The  $W(r)$  potential is taken in the Woods-Saxon form shown by

$$W(r) = -\frac{W_0}{1 + \exp\left(\frac{r-r_w(A_P^{1/3}+A_T^{1/3})}{a_w}\right)}, \quad (7)$$

where  $W_0$  is the depth,  $r_w$  is the radius, and  $a_w$  is diffuse-ness parameter. The double folding calculations have been performed by using the code DFPOT [9], and the elastic scattering cross-sections have been obtained with the help of the code FRESCO [10].

### 3. Density distributions of projectile and target nuclei

#### 3.1. Density distributions of projectile

##### 3.1.1. $Ngô$ - $Ngô$ density distribution

The  $Ngô$  -  $Ngô$  (Ngo) density is accepted as [11, 12]

$$\rho_i(r) = \frac{\rho_{0i}}{1 + \exp\left(\frac{r-C}{0.55}\right)}, \quad (i = n, p) \quad (8)$$

where

$$\begin{aligned} \rho_{0n(0p)} &= \frac{3}{4\pi} \frac{N(Z)}{A} \frac{1}{r_{0n(0p)}^3}, & C &= R \left(1 - \frac{1}{R^2}\right), \\ R &= \frac{NR_n + ZR_p}{A}, \end{aligned} \quad (9)$$

and

$$\begin{aligned} R_n &= (1.1375 + 1.875 \times 10^{-4} A) A^{1/3}, \\ R_p &= 1.128 A^{1/3}. \end{aligned} \quad (10)$$

##### 3.1.2. São Paulo density distribution

São Paulo (SP) density [13] is evaluated as the two-parameter Fermi (2pF)

$$\rho_i(r) = \frac{\rho_{0i}}{1 + \exp\left(\frac{r-R_i}{a_i}\right)}, \quad (i = n, p) \quad (11)$$

where

$$R_n = 1.49 N^{1/3} - 0.79, \quad a_n = 0.47 + 0.00046 N, \quad (12)$$

$$R_p = 1.81 Z^{1/3} - 1.12, \quad a_p = 0.47 - 0.00083 Z. \quad (13)$$

##### 3.1.3. Fermi density distribution

This density distribution is in the same form with SP density except for the values of  $R_{n(p)}$  and  $a_{n(p)}$  parameters given in the following form [14]

$$\begin{aligned} R_n &= 0.953 N^{1/3} + 0.015 Z + 0.774, \\ a_n &= 0.446 + 0.0072 \left(\frac{N}{Z}\right), \end{aligned} \quad (14)$$

$$R_p = 1.322 Z^{1/3} + 0.007 N + 0.022,$$

$$a_p = 0.449 + 0.0071 \left(\frac{Z}{N}\right). \quad (15)$$

This density is displayed as 2pF in our study.

#### 3.1.4. Gupta density distribution 1

This density distribution which is shown as G1 is parameter-ized by [15, 16]

$$\begin{aligned} \rho_i(r) &= \frac{\rho_{0i}}{1 + \exp\left(\frac{r-R_{0i}}{a_i}\right)}, \\ \rho_{0i} &= \frac{3A_i}{4\pi R_{0i}^3} \left(1 + \frac{\pi^2 a_i^2}{R_{0i}^2}\right)^{-1}, \end{aligned} \quad (16)$$

where

$$\begin{aligned} R_{0i} &= 0.90106 + 0.10957 A_i - 0.0013 A_i^2 \\ &+ 7.71458 \times 10^{-6} A_i^3 - 1.62164 \times 10^{-8} A_i^4, \end{aligned} \quad (17)$$

$$\begin{aligned} a_i &= 0.34175 + 0.01234 A_i - 2.1864 \times 10^{-4} A_i^2 \\ &+ 1.46388 \times 10^{-6} A_i^3 - 3.24263 \times 10^{-9} A_i^4. \end{aligned} \quad (18)$$

#### 3.1.5. Gupta density distribution 2

Gupta *et al.* [17] have reported different values of  $R_{0i}$  and  $a_i$  which are shown by

$$\begin{aligned} R_{0i} &= 0.9543 + 0.0994 A_i - 9.8851 \times 10^{-4} A_i^2 \\ &+ 4.8399 \times 10^{-6} A_i^3 - 8.4366 \times 10^{-9} A_i^4, \end{aligned} \quad (19)$$

$$\begin{aligned} a_i &= 0.3719 + 0.0086 A_i - 1.1898 \times 10^{-4} A_i^2 \\ &+ 6.1678 \times 10^{-7} A_i^3 - 1.0721 \times 10^{-9} A_i^4. \end{aligned} \quad (20)$$

This density is assigned as G2.

#### 3.1.6. Schechter density distribution

Schechter (S) density [18] which is in the 2pF form is dis-played by

$$\begin{aligned} \rho_0 &= \frac{0.212}{1 + 2.66 A^{-2/3}}, & R_0 &= 1.04 A^{1/3}, \\ a &= 0.54 \text{ fm}. \end{aligned} \quad (21)$$

### 3.1.7. Three parameters Fermi density distribution

Three parameters Fermi (3pF) density are written as

$$\rho_{3pF}(r) = \frac{\rho_0(1 + \frac{wr^2}{c^2})}{1 + \exp(\frac{r-c}{z})}, \quad (22)$$

where  $\rho_0 = 0.1816 \text{ fm}^{-3}$ ,  $w = -0.213$ ,  $c = 3.441 \text{ fm}$ , and  $z = 0.624 \text{ fm}$  [19, 20].

### 3.1.8. Hartree-Fock-Bogolubov density distribution

The last density investigated for  $^{32}\text{S}$  is the Hartree-Fock-Bogolubov model based on the BSk2 Skyrme force calculations [21]. This density distribution is taken from RIPL-3 [21] and is indicated as HFB in our work.

## 3.2. Density distributions of target nuclei

The elastic scattering cross sections of  $^{32}\text{S}$  from eleven different targets such as  $^{12}\text{C}$ ,  $^{27}\text{Al}$ ,  $^{40}\text{Ca}$ ,  $^{48}\text{Ca}$ ,  $^{48}\text{Ti}$ ,  $^{58}\text{Ni}$ ,  $^{63}\text{Cu}$ ,  $^{64}\text{Ni}$ ,  $^{76}\text{Ge}$ ,  $^{96}\text{Mo}$ , and  $^{100}\text{Mo}$  have been calculated. In this sense, the density of  $^{12}\text{C}$  target is formed by

$$\rho(r) = (\xi + \gamma r^2) \exp(-\beta r^2), \quad (23)$$

where  $\xi=0.1644$ ,  $\gamma=0.082003$ ,  $\beta=0.3741$  [22]. The density distribution of  $^{48}\text{Ca}$  nucleus is taken as the 3pF density shown by

$$\rho(r) = \frac{\rho_0 \left(1 + \frac{wr^2}{c^2}\right)}{1 + \exp(\frac{r-c}{z})}, \quad (24)$$

where  $\rho_0$ ,  $w$ ,  $c$ , and  $z$  are 0.173242, -0.03, 3.837, and 0.550, respectively [23]. The density distributions of  $^{27}\text{Al}$ ,  $^{40}\text{Ca}$ ,  $^{48}\text{Ti}$ ,  $^{58}\text{Ni}$ ,  $^{63}\text{Cu}$ ,  $^{64}\text{Ni}$ ,  $^{76}\text{Ge}$ ,  $^{96}\text{Mo}$  and  $^{100}\text{Mo}$  targets are obtained by using the 2pF density in the following form

$$\rho(r) = \frac{\rho_0}{1 + \exp(\frac{r-c}{z})}, \quad (25)$$

where  $\rho_0$ ,  $c$ , and  $z$  parameters are listed in Table I.

TABLE I. The parameters of two-parameter Fermi (2pF) density for the  $^{27}\text{Al}$ ,  $^{40}\text{Ca}$ ,  $^{48}\text{Ti}$ ,  $^{58}\text{Ni}$ ,  $^{63}\text{Cu}$ ,  $^{64}\text{Ni}$ ,  $^{76}\text{Ge}$ ,  $^{96}\text{Mo}$  and  $^{100}\text{Mo}$  nuclei.

2pF				
Nucleus	$c$	$z$	$\rho_0$	Ref.
$^{27}\text{Al}$	2.84	0.569	0.2015	[24]
$^{40}\text{Ca}$	3.60	0.523	0.169	[22]
$^{48}\text{Ti}$	3.75	0.567	0.17729	[24]
$^{58}\text{Ni}$	4.094	0.54	0.172	[22]
$^{63}\text{Cu}$	4.214	0.586	0.16877	[24]
$^{64}\text{Ni}$	4.285	0.584	0.1642	[24]
$^{76}\text{Ge}$	4.56508	0.551152	0.166727	[15,16]
$^{96}\text{Mo}$	4.88701	0.531139	0.175858	[15,16]
$^{100}\text{Mo}$	5.389	0.540	0.17219934	[25]

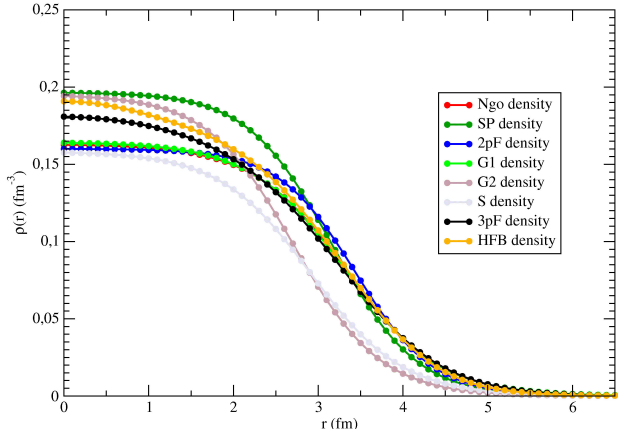


FIGURE 1. The changes as a function of distance ( $r$ ) of Ngo, SP, 2pF, G1, G2, S, 3pF and HFB density distributions in a linear scale.

## 4. Results and Discussion

### 4.1. Analysis with density distributions

The theoretical analysis of elastic scattering angular distributions of  $^{32}\text{S}$  projectile by  $^{12}\text{C}$ ,  $^{27}\text{Al}$ ,  $^{40}\text{Ca}$ ,  $^{48}\text{Ca}$ ,  $^{48}\text{Ti}$ ,  $^{58}\text{Ni}$ ,  $^{63}\text{Cu}$ ,  $^{64}\text{Ni}$ ,  $^{76}\text{Ge}$ ,  $^{96}\text{Mo}$ , and  $^{100}\text{Mo}$  targets have been performed for eight different density distributions of  $^{32}\text{S}$  indicated as Ngo, SP, 2pF, G1, G2, S, 3pF and HFB. The theoretical calculations have been carried out by using the double folding model based on the optical model. The change of each density distribution by distance ( $r$ ) is shown in Fig. 1. We can see that SP density has the highest density in the center part, while S density has the lowest density. It can be also observed that all the densities lie around nuclear saturation density. Moreover, the root mean square (rms) radii of these densities are given in Table II as compared with those presented in the literature.

The imaginary potential parameters have been studied to produce results in good agreement with the experimental data. Although it is very difficult to study on the same potential geometry for different reactions and different density distributions, this method has been preferred in our study. This is because both global equations of the imaginary potential depths and better physical inference are to be presented. For this aim,  $W_0$ ,  $r_w$  and  $a_w$  parameters which define the Woods-Saxon potential have been determined by using the following processes; i)  $r_w$  parameter is determined by varying at 0.1 and 0.01 fm interval at fixed  $W_0$  and  $a_w$  values, ii)  $a_w$  parameter is determined by varying at 0.1 and 0.01 fm interval at fixed  $W_0$  and  $r_w$  values, iii)  $W_0$  parameter is obtained for fixed  $r_w$  and  $a_w$  values. Thus,  $r_w$  and  $a_w$  values have been taken as 1.30 fm and 0.41 fm, respectively.

In our study, we have divided our discussion as the reactions with light, medium, and heavy mass targets. In this context, as for light and light-medium target samples, we have analyzed  $^{32}\text{S} + ^{12}\text{C}$  reaction at  $E_{\text{lab}} = 110 \text{ MeV}$ ,  $^{32}\text{S} + ^{27}\text{Al}$

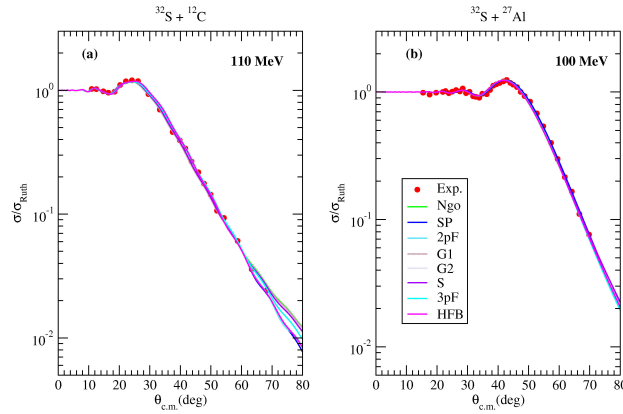


FIGURE 2. The elastic scattering cross sections calculated by using Ngo, SP, 2pF, G1, G2, S, 3pF, and HFB densities of  $^{32}\text{S}$  projectile for (a)  $^{32}\text{S} + ^{12}\text{C}$  at  $E_{\text{lab}}=110$  MeV, and (b)  $^{32}\text{S} + ^{27}\text{Al}$  at  $E_{\text{lab}}=100$  MeV. The experimental data are taken from Ref. [31,32].

TABLE II. The rms radii of Ngo, SP, 2pF, G1, G2, S, 3pF, and HFB density distributions as compared with the literature.

Density distribution	rms radii (fm)
Ngo	3.290
SP	3.033
2pF	3.155
G1	3.297
G2	3.243
S	3.251
3pF	3.236
HFB	3.168
Literature	3.263(2) <sup>a</sup> , 3.323 <sup>b</sup> , 3.245 $\pm$ 0.032 <sup>c</sup> $3.244 \pm 0.018^d$ , 3.26 <sup>e</sup>

<sup>a</sup> Determined via Ref. [26]. <sup>b</sup> Determined via Ref. [27].

<sup>c</sup> Determined via Ref. [28]. <sup>d</sup> Determined muonic x-ray value [29].

<sup>e</sup> Determined via Ref. [30].

reaction at  $E_{\text{lab}}=100$  MeV,  $^{32}\text{S} + ^{40}\text{Ca}$  reaction at  $E_{\text{lab}}=100$  MeV,  $^{32}\text{S} + ^{48}\text{Ca}$  reaction at  $E_{\text{lab}}=83.3$  MeV, and  $^{32}\text{S} + ^{48}\text{Ti}$  reaction at  $E_{\text{lab}}=160$  MeV. In Fig. 2 we present the elastic scattering cross sections for  $^{32}\text{S} + ^{12}\text{C}$  and  $^{32}\text{S} + ^{27}\text{Al}$  reactions, and in Fig. 3 for  $^{32}\text{S} + ^{40}\text{Ca}$ ,  $^{32}\text{S} + ^{48}\text{Ca}$ , and  $^{32}\text{S} + ^{48}\text{Ti}$  reactions. Besides, we have calculated the  $\chi^2/N$  values for each density distribution, and have listed them in Table III. The 3pF density for  $^{32}\text{S} + ^{12}\text{C}$  reaction and the SP density for  $^{32}\text{S} + ^{27}\text{Al}$  reaction are slightly better than the other densities. The Ngo density for  $^{32}\text{S} + ^{40}\text{Ca}$  reaction, the SP density for  $^{32}\text{S} + ^{48}\text{Ca}$  reaction and the HFB density for  $^{32}\text{S} + ^{48}\text{Ti}$  reaction are in slightly better agreement with the experimental data compared to other densities.

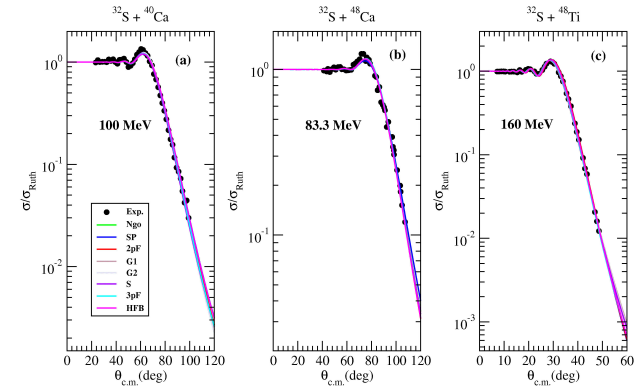


FIGURE 3. Same as Fig. 2, but for (a)  $^{32}\text{S} + ^{40}\text{Ca}$  at  $E_{\text{lab}}=100$  MeV, (b)  $^{32}\text{S} + ^{48}\text{Ca}$  at  $E_{\text{lab}}=83.3$  MeV, and (c)  $^{32}\text{S} + ^{48}\text{Ti}$  at  $E_{\text{lab}}=160$  MeV. The experimental data are taken from Ref. [33,34].

As regards medium mass target reaction samples, we have calculated the elastic scattering cross sections of  $^{32}\text{S} + ^{58}\text{Ni}$  reaction at  $E_{\text{lab}}=97.3$  MeV,  $^{32}\text{S} + ^{63}\text{Cu}$  reaction at  $E_{\text{lab}}=168$  MeV,  $^{32}\text{S} + ^{64}\text{Ni}$  reaction at  $E_{\text{lab}}=150$  MeV and  $^{32}\text{S} + ^{76}\text{Ge}$  reaction at  $E_{\text{lab}}=178$  MeV. We have compared the theoretical results and the experimental data in Fig. 4. For  $^{32}\text{S} + ^{58}\text{Ni}$  reaction, it has been observed that the SP density is better than the others while the density distributions investigated are in good agreement with the data. The Ngo and G1 densities for  $^{32}\text{S} + ^{63}\text{Cu}$  reaction, the 2pF density for  $^{32}\text{S} + ^{64}\text{Ni}$  reaction, and the 2pF density for  $^{32}\text{S} + ^{76}\text{Ge}$  reaction are slightly better than the other densities.

As for heavy target nucleus samples, we have calculated the elastic scattering cross-sections of  $^{32}\text{S} + ^{96}\text{Mo}$  reaction and  $^{32}\text{S} + ^{100}\text{Mo}$  reaction at  $E_{\text{lab}}=180$  MeV. We have displayed the theoretical results in Fig. 5. For  $^{32}\text{S} + ^{96}\text{Mo}$  reaction, we observe that the results of SP and 2pF densities are highly consistent with the data. We notice that the results of 2pF density distribution are better than the results of other densities. For  $^{32}\text{S} + ^{100}\text{Mo}$  reaction, we notice that density distributions generally exhibit unstable behaviors with each other. However, it has been found that SP density distribution is quite compatible with the experimental data from the comparison of all density distributions.

#### 4.2. Interpretation of normalization constant, reaction cross-section and volume integrals

The normalization constant ( $N_R$ ) is a parameter used in the double folding model to increase the agreement between experimental data and theoretical results. The default value of this parameter is 1.0. However, the deviation from this value may be due to either uncertainty or peculiarity of experimental data or the fitting process of theoretical calculations. We display the  $N_R$  values against  $E/A_P$  for the analyzed reactions by using eight various densities of the  $^{32}\text{S}$  nucleus in Fig. 6. The results are sensitive to  $N_R$  constant, and the  $N_R$  value has been found to be around unity in heavy nucleus reactions. The results for the medium, heavy targets are very sensitive to the value of  $N_R$ , and the deviation is high, espe-

TABLE III. The  $\chi^2/N$  values calculated for Ngo, SP, 2pF, G1, G2, S, 3pF, and HFB density distributions.

Target nucleus	$E_{\text{Lab}}$ (MeV)	$(\frac{\chi^2}{N})_{\text{Ngo}}$	$(\frac{\chi^2}{N})_{\text{SP}}$	$(\frac{\chi^2}{N})_{\text{2pF}}$	$(\frac{\chi^2}{N})_{\text{G1}}$	$(\frac{\chi^2}{N})_{\text{G2}}$	$(\frac{\chi^2}{N})_{\text{S}}$	$(\frac{\chi^2}{N})_{\text{3pF}}$	$(\frac{\chi^2}{N})_{\text{HFB}}$
$^{12}\text{C}$	110	0.26	0.22	0.25	0.25	0.15	0.15	0.12	0.20
$^{27}\text{Al}$	100	0.16	0.07	0.14	0.14	0.14	0.12	0.15	0.15
$^{40}\text{Ca}$	100	0.42	0.85	0.69	0.64	0.68	0.44	0.53	0.81
$^{48}\text{Ca}$	83.3	0.33	0.32	0.40	0.34	0.35	0.36	0.40	0.39
$^{48}\text{Ti}$	160	0.28	0.38	0.32	0.36	0.25	0.25	0.18	0.12
$^{58}\text{Ni}$	97.3	0.62	0.37	0.52	0.53	0.55	0.52	0.54	0.62
$^{63}\text{Cu}$	168	1.37	1.41	1.40	1.37	1.40	1.42	1.43	1.41
$^{64}\text{Ni}$	150	1.73	1.00	0.97	1.53	1.47	1.51	1.53	1.00
$^{76}\text{Ge}$	178	0.58	0.47	0.34	0.56	0.51	0.52	0.37	0.39
$^{96}\text{Mo}$	180	0.53	0.29	0.23	0.60	0.45	0.61	0.34	0.43
$^{100}\text{Mo}$	180	4.20	0.44	1.01	4.77	3.08	2.94	1.17	1.83

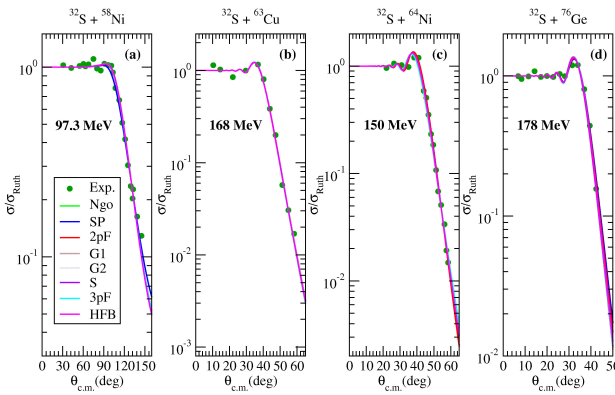


FIGURE 4. Same as Fig. 2, but for (a)  $^{32}\text{S} + ^{58}\text{Ni}$  at  $E_{\text{lab}}=97.3$  MeV, (b)  $^{32}\text{S} + ^{63}\text{Cu}$  at  $E_{\text{lab}}=168$  MeV, (c)  $^{32}\text{S} + ^{64}\text{Ni}$  at  $E_{\text{lab}}=150$  MeV, and (d)  $^{32}\text{S} + ^{76}\text{Ge}$  at  $E_{\text{lab}}=178$  MeV. The experimental data are taken from Ref. [35–38].

cially in  $^{32}\text{S} + ^{63}\text{Cu}$  reaction. One of the reasons can be due to the study performed by using the same potential geometry for all density distributions and reactions.

The real ( $J_v$ ) and imaginary ( $J_w$ ) volume integrals for eight different density distributions have been calculated, and the changes of volume integrals against  $E/A_P$  are displayed in Fig. 7. The largest  $J_v$  values have been obtained for the SP density, and the smallest  $J_v$  values for the G1 density. One of the main reasons for this fact is that the  $N_R$  values obtained according to the SP density are larger than those obtained according to other densities, whereas the  $N_R$  values obtained according to G1 density are smaller than those obtained according to other densities. Anyway, the  $J_v$  values of other densities are closer to each other. On the other hand, the imaginary potential parameters are effective on  $J_w$  volume integrals. While the  $J_w$  values of the density distributions are generally close to each other, in some cases, they vary according to the values of the imaginary potential parameters.

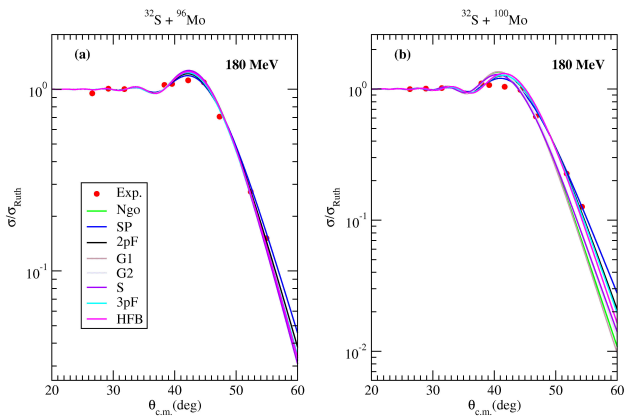


FIGURE 5. Same as Fig. 2, but for (a)  $^{32}\text{S} + ^{96}\text{Mo}$  at  $E_{\text{lab}}=180$  MeV, and (b)  $^{32}\text{S} + ^{100}\text{Mo}$  at  $E_{\text{lab}}=180$  MeV. The experimental data are taken from Ref. [39].

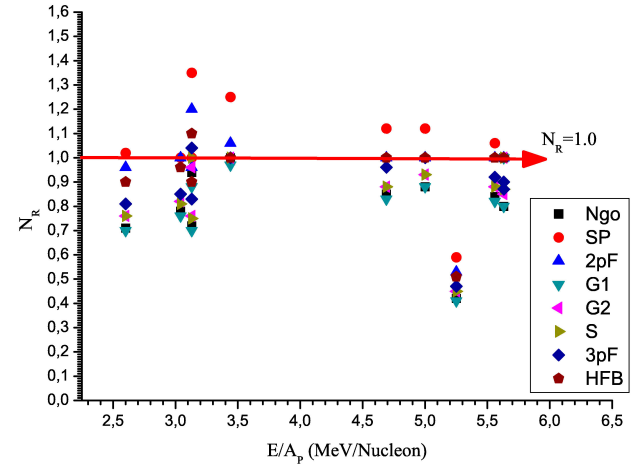
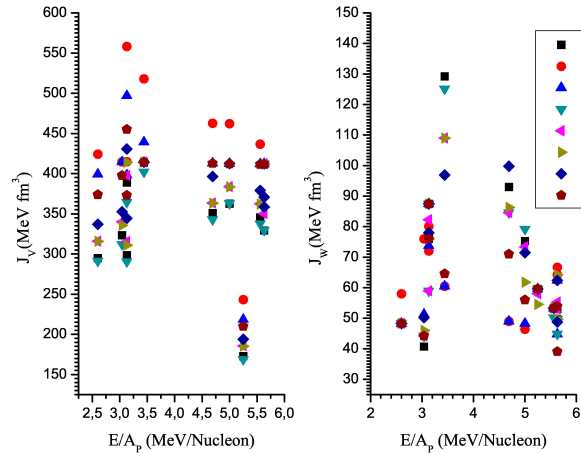


FIGURE 6. The normalization values ( $N_R$ ) for the calculations with Ngo, SP, 2pF, G1, G2, S, 3pF, and HFB densities versus  $E/A_P$ .

TABLE IV. The cross-sections (in mb) obtained for Ngo, SP, 2pF, G1, G2, S, 3pF, and HFB density distributions.

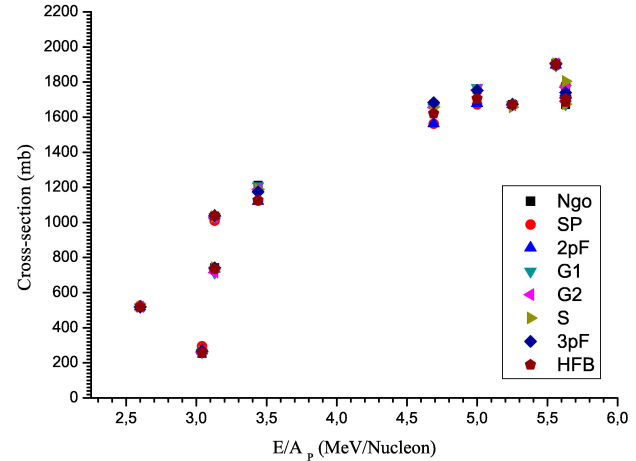
Target nucleus	$E_{\text{Lab}}$ (MeV)	$\sigma_{\text{Ngo}}$ (mb)	$\sigma_{\text{SP}}$ (mb)	$\sigma_{\text{2pF}}$ (mb)	$\sigma_{\text{G1}}$ (mb)	$\sigma_{\text{G2}}$ (mb)	$\sigma_{\text{S}}$ (mb)	$\sigma_{\text{3pF}}$ (mb)	$\sigma_{\text{HFB}}$ (mb)
$^{12}\text{C}$	110	1212	1124	1121	1208	1189	1189	1174	1126
$^{27}\text{Al}$	100	1036	1010	1039	1034	1029	1034	1039	1038
$^{40}\text{Ca}$	100	743	740	734	714	715	743	741	735
$^{48}\text{Ca}$	83.3	517	527	520	518	518	519	518	520
$^{48}\text{Ti}$	160	1759	1672	1679	1768	1755	1751	1752	1706
$^{58}\text{Ni}$	97.3	254	295	269	260	260	262	266	259
$^{63}\text{Cu}$	168	1672	1671	1672	1672	1668	1657	1673	1672
$^{64}\text{Ni}$	150	1672	1563	1564	1656	1655	1658	1683	1621
$^{76}\text{Ge}$	178	1906	1893	1898	1895	1905	1905	1903	1903
$^{96}\text{Mo}$	180	1672	1712	1707	1673	1691	1674	1710	1686
$^{100}\text{Mo}$	180	1775	1780	1738	1763	1770	1804	1739	1704

FIGURE 7. The real and imaginary volume integrals for the calculations with Ngo, SP, 2pF, G1, G2, S, 3pF, and HFB densities versus  $E/A_p$ .

The reaction cross-section ( $\sigma_R$ ) is one of the important parameters sought in the reactions analyzed. In this context, cross-section values close to each other for different optical model calculations can be an indication of the suitability of the fitting process applied to the experimental data. The  $\sigma_R$  values of all the reactions and for each density distribution are given as compared in Table IV, and are plotted as a function of  $E/A_p$  in Fig. 8. We can remark that the  $\sigma_R$  values obtained for different densities are in agreement with each other.

#### 4.3. New and global analytical expressions of imaginary potential depths

Different theoretical models are used to explain the experimental data of nuclear reactions. For this, it is necessary to identify suitable potentials that well define the colliding system. In this context, the optical model is quite valid in ex-

FIGURE 8. The cross-sections (in mb) for the calculations with Ngo, SP, 2pF, G1, G2, S, 3pF, and HFB densities versus  $E/A_p$ .

plaining the different nuclear interactions. The potential of this model consists of two parts, real and imaginary. In our study, real potential has been obtained with the double folding model. To determine the imaginary potential of the  $^{32}\text{S}$  nucleus, new and global analytical expressions are proposed by using the elastic scattering results of different nuclear interactions and density distributions. Thus, these equations can be used as input to the analysis of different reactions. The expressions are formulated as

$$\text{Ngo density} \rightarrow W^{Ngo} = 23.24 + 0.15E - \frac{1.26Z_T}{A_T^{1/3}} \quad (26)$$

$$\text{SP density} \rightarrow W^{SP} = 11.35 - 0.13E + \frac{6.16Z_T}{A_T^{1/3}} \quad (27)$$

$$\text{2pF density} \rightarrow W^{2pF} = 12.62 - 0.02E + \frac{3.21Z_T}{A_T^{1/3}} \quad (28)$$

$$\text{G1 density} \rightarrow W^{G1} = 22.01 + 0.15E - \frac{1.41Z_T}{A_T^{1/3}} \quad (29)$$

$$\text{G2 density} \rightarrow W^{G2} = 15.45 + 0.14E - \frac{0.13Z_T}{A_T^{1/3}} \quad (30)$$

$$\text{S density} \rightarrow W^S = 18.52 + 0.08E + \frac{0.76Z_T}{A_T^{1/3}} \quad (31)$$

$$\text{3pF density} \rightarrow W^{3pF} = 17.63 + 0.08E + \frac{1.10Z_T}{A_T^{1/3}} \quad (32)$$

$$\text{HFB density} \rightarrow W^{HFB} = 17.36 + 0.02E + \frac{1.68Z_T}{A_T^{1/3}} \quad (33)$$

where  $E$  is the incident energy,  $Z_T$  is an atomic number of targets, and  $A_T$  is mass number of targets.

## 5. Summary and Conclusions

Our study has been carried out in two steps. In the first one, elastic scattering cross-sections of the  $^{32}\text{S}$  projectile from

$^{12}\text{C}$ ,  $^{27}\text{Al}$ ,  $^{40}\text{Ca}$ ,  $^{48}\text{Ca}$ ,  $^{48}\text{Ti}$ ,  $^{58}\text{Ni}$ ,  $^{63}\text{Cu}$ ,  $^{64}\text{Ni}$ ,  $^{76}\text{Ge}$ ,  $^{96}\text{Mo}$ , and  $^{100}\text{Mo}$  target nuclei have been calculated at various incident energies. For this purpose, eight density distributions of  $^{32}\text{S}$  have been used. The theoretical results have been compared with both each other and experimental data. It has been observed that the density distributions examined in our study have given a general agreement in explaining the experimental data. Additionally, Ngo, SP, 3pF, and HFB densities for light mass target reactions, Ngo, SP, 2pF, and G1 densities for medium mass target reactions, and 2pF and SP densities for heavy mass target reactions are more suitable than other density distributions.

In the second step, the imaginary potential for each density distribution has been obtained by means of the potential parameters used in the  $^{32}\text{S}$  elastic scattering calculations. These analytical expressions vary depending on the incident energy of the projectile, the atomic number, and the mass number of the target nucleus. Thus, these equations will be useful in the analysis of reactions concerning  $^{32}\text{S}$  nuclei such as elastic scattering, inelastic scattering, transfer reactions with both broadly different target nuclei, and incident energies.

## Acknowledgments

Authors thank the referee for valuable comments.

- 
1. <https://www.nndc.bnl.gov/nudat2/>
  2. <https://www.tracesciences.com/s.htm>
  3. M. Aygun, O. Kocadag and Y. Sahin, *Rev. Mex. Fis.* **61** (2015) 414-420.
  4. M. Aygun, *Rev. Mex. Fis.* **62** (2016) 336-343.
  5. M. Aygun and Z. Aygun *Rev. Mex. Fis.* **65** (2019) 404-411.
  6. M. Aygun, *Braz. J. Phys.* **49** (2019) 760-771. <https://doi.org/10.1007/s13538-019-00680-7>
  7. M. Aygun, *Pramana - J. Phys.* **93** (2019) 72. <https://doi.org/10.1007/s12043-019-1835-y>
  8. G.R. Satchler, *Direct Nuclear Reactions*, Oxford University Press, Oxford, 1983.
  9. J. Cook, *Commun. Comput. Phys.* **25** (1982) 125-139.
  10. I.J. Thompson, *Comput. Phys. Rep.* **7** (1988) 167. [https://doi.org/10.1016/0167-7977\(88\)90005-6](https://doi.org/10.1016/0167-7977(88)90005-6)
  11. C. Ngô *et al.*, *Nucl. Phys. A* **252** (1975) 237. [https://doi.org/10.1016/0375-9474\(75\)90614-4](https://doi.org/10.1016/0375-9474(75)90614-4)
  12. H. Ngô and C. Ngô, *Nucl. Phys. A* **348** (1980) 140.
  13. L.C. Chamon *et al.*, *Phys. Rev. C* **66** (2002) 014610. <https://doi.org/10.1103/PhysRevC.66.014610>
  14. W.M. Seif and H. Mansour, *Int. J. Mod. Phys. E* **24** (2015) 1550083. <https://doi.org/10.1142/S0218301315500834>
  15. R.K. Gupta, D. Singh and W. Greiner, *Phys. Rev. C* **75** (2007) 024603. <https://doi.org/10.1103/PhysRevC.75.024603>
  16. O.N. Ghodsi and F. Torabi, *Phys. Rev. C* **92** (2015) 064612. <https://doi.org/10.1103/PhysRevC.92.064612>
  17. R.K. Gupta, D. Singh, R. Kumar and W. Greiner, *J. Phys. G: Nucl. Part. Phys.* **36** (2009) 075104. <https://doi.org/10.1088/0954-3899/36/7/075104>
  18. H. Schechter and L.F. Canto, *Nucl. Phys. A* **315** (1979) 470. [https://doi.org/10.1016/0375-9474\(79\)90623-7](https://doi.org/10.1016/0375-9474(79)90623-7)
  19. G.C. Li, M.R. Yearian and I. Sick, *Phys. Rev. C* **9** (1974) 1861. <https://doi.org/10.1103/PhysRevC.9.1861>
  20. A.K. Hamoudi, *ANJS* **13** (2012) 105-113.
  21. <http://www-nds.iaea.org/ripl-2.html>.
  22. M. El-Azab Farid and M.A. Hassanain, *Nucl. Phys. A* **678** (2000) 39. [https://doi.org/10.1016/S0375-9474\(00\)00313-4](https://doi.org/10.1016/S0375-9474(00)00313-4)
  23. G.D. Alkhazov *et al.*, *Nucl. Phys. A* **280** (1977) 365. [https://doi.org/10.1016/0375-9474\(77\)90611-X](https://doi.org/10.1016/0375-9474(77)90611-X)
  24. C.W. De Jager, H. De Vries and C. De Vries, *At. Data Nucl. Data Tables* **14** (1974) 479. [https://doi.org/10.1016/0092-640X\(87\)90013-1](https://doi.org/10.1016/0092-640X(87)90013-1)
  25. W. Zou, Y. Tian and Z.Yu. Ma, *Phys. Rev. C* **78** (2008) 064613.

- 26. L.A. Schaller *et al.*, *Nucl. Phys. A* **300** (1978) 225. [https://doi.org/10.1016/0375-9474\(78\)96128-6](https://doi.org/10.1016/0375-9474(78)96128-6)
- 27. J. Streets, B.A. Brown and P.E. Hodgson, *J. Phys. G: Nucl. Phys.* **8** (1982) 839-850. <https://doi.org/10.1088/0305-4616/8/6/013>
- 28. G.C. Li, I. Sick and M.R. Yearian, *Phys. Lett. B* **37** (1971) 282. [https://doi.org/10.1016/0370-2693\(71\)90019-0](https://doi.org/10.1016/0370-2693(71)90019-0)
- 29. C.S. Wu and L. Willets, *Ann. Rev. Nucl. Sci.* **19** (1969) 527. <https://doi.org/10.1146/annurev.ns.19.120169.002523>
- 30. I. Angeli and K.P. Marinova, *At. Data Nucl. Data Tables* **99** (2013) 69. <https://doi.org/10.1016/j.adt.2011.12.006>
- 31. N. Arena *et al.*, *Il Nuovo Cimento* **100** (1988) 6. <https://doi.org/10.1007/BF02789013>
- 32. J.D. Garrett *et al.*, *Phys. Rev. C* **12** (1975) 489. <https://doi.org/10.1103/PhysRevC.12.489>
- 33. G.R. Satchler and W.G. Love, *Phys. Report* **55** (1979) 183-254. [https://doi.org/10.1016/0370-1573\(79\)90081-4](https://doi.org/10.1016/0370-1573(79)90081-4)
- 34. F. Porto *et al.*, *Nucl. Phys. A* **351** (1981) 237-245. [https://doi.org/10.1016/0375-9474\(81\)90639-9](https://doi.org/10.1016/0375-9474(81)90639-9)
- 35. A.M. Stefanini *et al.*, *Phys. Rev. C* **41** (1990) 1018. <https://doi.org/10.1103/PhysRevC.41.1018>
- 36. S. Agnoli *et al.*, *Nucl. Phys. A* **464** (1987) 103-124. [https://doi.org/10.1016/0375-9474\(87\)90425-8](https://doi.org/10.1016/0375-9474(87)90425-8)
- 37. A.M. Stefanini *et al.*, *Phys. Rev. Lett.* **59** (1987) 2852. <https://doi.org/10.1103/PhysRevLett.59.2852>
- 38. G. Guillaume *et al.*, *Phys. Rev. C* **26** (1982) 2458. <https://doi.org/10.1103/PhysRevC.26.2458>
- 39. D.M. Herrick *et al.*, *Phys. Rev. C* **52** (1995) 744. <https://doi.org/10.1103/PhysRevC.52.744>